Ultrahigh Field Enhancement and Photoresponse in Atomically Separated Arrays of Plasmonic Dimers

*Debadrita Paria, Kallol Roy, Haobijam Johnson Singh, Shishir Kumar, Srinivasan Raghavan, Arindam Ghosh, and Ambarish Ghosh**

The large concentration of electromagnetic (EM) fields near metal nanoparticles upon illumination of light is one of the defining concepts of light matter interactions at the nanoscale.[1,2] The strength of this so-called "near field" can be very large at the junction of two metal nanoparticles, which has facilitated promising technologies, such as the detection of single molecules,[3,4] through a large enhancement of the Raman scattering signal. The degree of enhancement of the near field increases rapidly as the particles are brought closer, thereby suggesting an atomically thin and uniform material, such as graphene, as the ideal spacer layer for maximum near field enhancement. Here we combine oblique angle deposition (OAD) technique with standard graphene transfer protocols to fabricate two metal nanoparticle arrays separated precisely by a single layer of graphene (SLG). Upon illumination of light of appropriate wavelength, the optical near field at the junction of the particles could be strongly enhanced which was reflected in an order of magnitude increase of the Raman signal of the graphene monolayer. Most crucially, the enhanced near field resulted in a dramatic increase of photoresponse in graphene[5] that allowed the realization of a new class of large-area color-selective plasmonic photodetectors. At room temperature, the maximum responsivity of these devices approached 2 A W^{-1}, nearly two orders of magnitude greater than that of the of previous graphene-based plasmonic devices, which signify the tremendous promise of this novel method of integrating plasmonics with graphene and other atomically thin materials.

When two nanoparticles made of noble metals under appropriate illumination are placed within few nm of each other, the EM field induced at their junction can get amplified by several orders of magnitude, thereby facilitating two technologies of immense current interest. These so-called "hot spots" have facilitated the detection of single molecules through surface enhanced Raman spectroscopy (SERS),[3,4,6–8] which in turn inspired an entire field of research devoted to the development of substrates containing metallic structures with nanosized gaps in between. Beside SERS applications, the enhanced EM field at nanoparticle junctions can also be used to enhance the performance of various optoelectronic devices, such as those pertaining to photovoltaics[9] and high-speed wavelength-selective photodetection.

In electrostatics, the electric field between two oppositely charged plates varies inversely as the distance between them, which arises due to Coulomb interactions between the charges residing on the two plates. Similarly, the dependence of the EM field enhancement[10] on the size of the gap (d) originates in the EM interactions between the localized plasmon modes of two neighboring nanoparticles (radius a). In the simplest approximation, each particle can be approximated as an electric dipole $\vec{p_i}$, whose strength is proportional to the net electric field ($\vec{p_i} = a\vec{E_i}$) at its location, where a is the polarizabiltiy of the particle at the wavelength of illumination. The contributions to the net electric field for particle 1 come from the incident field ($\vec{E_0}$), as well as the electric field due to the dipole ($\vec{p_2}$) of particle 2 at the location of particle 1, where the dominant term of $\vec{E_2} \propto d^{-3}$, thus implying a strong distance dependence of the dipolar coupling. This approximation breaks down for $d < a$, beyond which higher order multipolar contributions needs to be taken into account, where numerical calculations can provide an accurate picture. Also important is the direction of propagation and state of polarization of the incident beam, and their relation to the interparticle axis. As an example, depicted schematically in **Figure 1**a, we have considered linearly polarized monochromatic light incident along the axis of the interparticle separation for two silver nanospheres of radius a = 70 nm separated by a distance d. The calculated value of the squared enhancement $(|E|/|E_o|)^2$ of the electric field, shows concentration of the electric field at the junction of the particles, which increases manifold as the distance d is reduced. The maximum value of the enhancement within the junction, given by $(|E|/|E_o|)^2_{max}$, depended strongly on the illumination wavelength and the interparticle separation, as can be seen in Figure 1b. The smallest d considered in these simulations corresponded to the thickness of single-layer graphene, which resulted in maximum value of $(|E|/|E_o|)^2 \geq 10^6$ in the wavelength regime 405 to 530 nm (approx), implying a system of plasmonic dimers with sub-nm separation can achieve the strongest EM field enhancements.

D. Paria, Dr. S. Kumar, Prof. S. Raghavan, Dr. A. Ghosh
Centre for Nano Science and Engineering
Indian Institute of Science
Bangalore 560012, India
E-mail: ambarish@ece.iisc.ernet.in
K. Roy, H. J. Singh, Prof. A. Ghosh, Dr. A. Ghosh
Department of Physics
Indian Institute of Science
Bangalore 560012, India
Prof. S. Raghavan
Materials Research Centre
Indian Institute of Science
Bangalore 560012, India
Dr. A. Ghosh
Department of Electrical Communications Engineering
Indian Institute of Science
Bangalore 560012, India

DOI: 10.1002/adma.201404312

ADVANCED MATERIALS
www.advmat.de

www.MaterialsViews.com

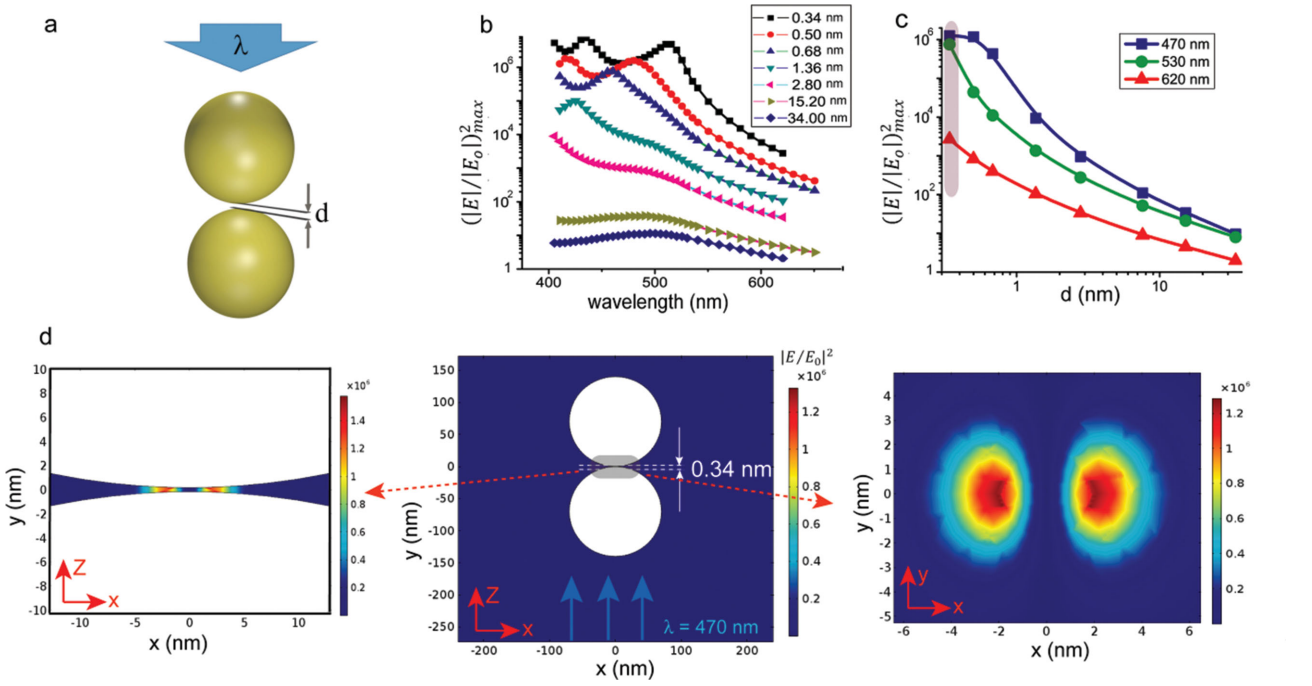

Figure 1. EM field enhancement. a) Light of wavelength λ, linearly polarized along the *x*-axis, incident along the interparticle axis (*z*-axis) of two silver nanospheres separated by a distance *d*. b) Spectral dependence of the maximum value of the enhanced field $(|E|/|E_o|)^2$ in the dimer junction for various *d* (labeled in nm). c) Dependence of the maximum enhancement $(|E|/|E_o|)^2_{max}$ at the dimer junction on the size of the gap $d = 0.34$ nm, for three illumination wavelengths. The particular choices of the wavelengths (red – 620 nm, green – 530 nm, and blue – 470 nm) were based on the colors of the LEDs used in the photoresponse experiments, which will be discussed in a later section of this manuscript. d) Strong EM field enhancement at the junction of the nanoparticles for $d = 0.34$ nm and incident light at 470 nm. The spatial variation of $(|E|/|E_o|)^2$ in the *x*–*z* plane ($y = 0$) and *x*–*y* plane ($z = 0$) are shown in left and right panels, respectively. Particularly important is the enhanced EM field in the plane perpendicular to the interparticle axis, (*x*–*y* plane), which is mostly concentrated in two elliptical lobes about the origin, with effective area $\sigma \approx 19$ nm^2 for incident light of wavelength 470 nm. See the Supporting Information for more details on the calculation of σ. All dimensions are in nm.

The distance dependence of $(|E|/|E_o|)^2_{max}$ for three illumination wavelengths is shown in Figure 1c.

The engineering challenges to develop such a system are primarily related to the smallest gap that can be reliably and reproducibly obtained with the chosen method of fabrication, with a possible emphasis towards the development of large area substrates using scalable techniques. Commonly used systems, such as aggregates of metal colloids, suffer from the randomness of the gap size and therefore the EM field enhancement, whereas the typical resolution[11] achievable with electron beam lithography being greater than 5 nm, renders standard lithographic approaches mostly ineffective. Among various wafer scale methods, the array of metallic nanopyramids obtained with nanosphere lithography[12] is common, although it suffers from the nonuniformity of the gap sizes below few nm. This is also true for recently reported[13] self-assembled pair of gold nanorods whose separations varied between 0.5 and 2 nm. Alternate approaches towards fabricating uniform and reproducible nm sized gaps have relied on using a thin spacer material, such as polyelectrolyte[14] coating (thickness > 3 nm) or SLG[15] (spacing 0.34 nm) separating a collection of gold colloids from a thin film, also made of gold. One shortcoming of this method is related to the conductivity of the underlying metal film, which makes this method incompatible with applications aiming towards improving the photodetection efficiency of the thin spacer material. The solution that presents itself is therefore not to use a gold film, but rather place a spacer material between a pair[16–18] of metal nanoparticles. For realistic applications requiring large area devices, an attractive possibility would be to use two arrays of plasmonic nanoparticles separated by a suitable spacer material, which by virtue of its large near field focusing, can be used as a sensitive SERS substrate, and as a photoresponsive device as well. As we demonstrate in this paper, an almost ideal solution can be achieved with a SLG acting as a spacer between two arrays of silver nanoparticles, giving rise to extremely large and localized EM fields, resulting in a 100-fold enhancement of the SLG photoresponse.

Three properties of graphene make it an ideal candidate as a spacer material: (i) graphene can be used as a standard for Raman[19–22] measurements, since its Raman scattering is highly reproducible and well understood. Additionally, it is possible to functionalize graphene with various chemicals, which in conjunction with the highly enhanced near field, allows graphene to be an ideal substrate for SERS measurements. (ii) In spite of its low absorption, graphene shows broadband and fast photoresponse, and therefore promising as a material for photodetection. (iii) Most importantly, it is one of the thinnest materials available, with thickness precisely that of an atom (0.34 nm), thereby allowing a very large enhancement of the EM field at the junction of the nanoparticles, as shown in Figure 1c. An important question that arises is whether this is the highest field enhancement one could achieve, or

DOI: 10.1002/adma.201404312

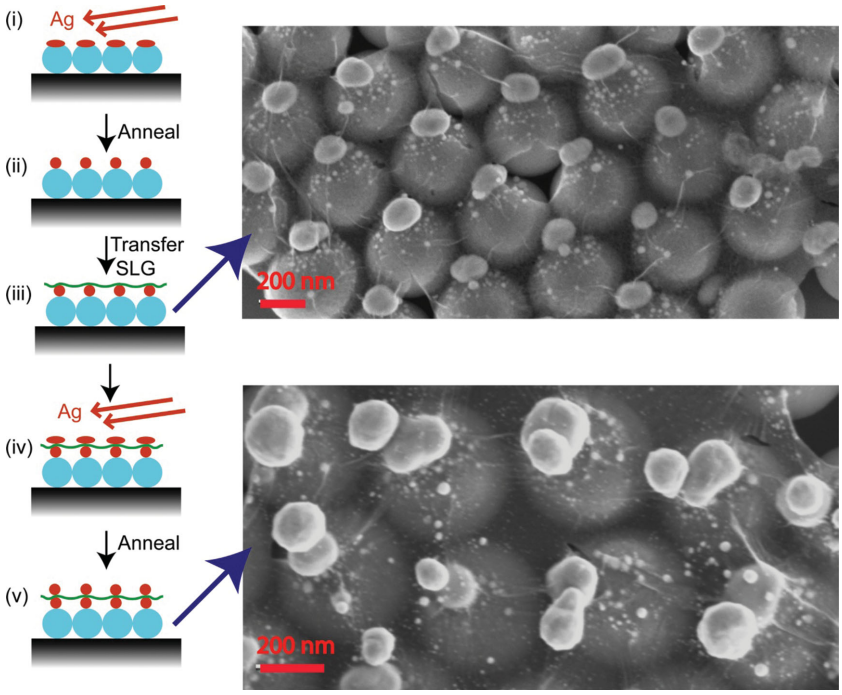

Figure 2. Method of fabrication. Schematic of the fabrication steps along with representative SEM images: i) OAD of silver on a monolayer of silica beads with the substrate at 80 K; ii) annealing the substrate to render the silver particles spherical; iii) transfer of SLG (SEM image shown); iv) second OAD of silver while keeping the substrate at 80 K; and (v) annealing the substrate to render the silver islands spherical (SEM image shown).

whether further reduction in the gap can result in even larger $(|E|/|E_o|)^2$. For the estimates shown in Figure 1, the nanoplasmonic system was assumed to follow classical electrodynamics in Drude local response approximation. For such tiny gaps, there could be significant contribution from nonlocal[23–27] response of the dimers, which could result in lower EM field enhancement with respect to the estimates obtained from local response approximation. Besides, for separations around 0.3–0.5 nm, quantum tunneling[28–30] of plasmons are predicted to limit the maximum enhancement of the optical fields at the junction, although similar effects have also been predicted by recent[31] semiclassical treatment of the nonlocal response. Taken together, single layer graphene appears as a near ideal spacer material for plasmonic dimers.

Achieving the proposed device architecture of a pair of 2D arrays of metal nanoparticles separated by SLG required the confluence of multiple fabrication schemes. While multiple protocols exist for large area assembly of colloidal particles and subsequent deposition of SLG, placing a nanoparticle array directly above another is not trivial.[32] In this work, this was achieved by OAD[33] of a metal film with active substrate cooling,[34] and subsequent annealing, a method that can be broadly classified as a type of directed self assembly. We chose the spacing between adjacent nanoparticles within an array to be quite large, similar to the wavelength of illumination used in the experiments reported here. Accordingly, we could neglect the plasmon interactions between neighboring dimers within the array, consistent with the assumptions made in the theoretical calculations shown in Figure 1b,c. The large interparticle separation also allowed us to image the large near field concentration at the colloidal junctions using Raman spectroscopy. The sequence of steps used for fabricating the metal arrays separated by graphene is shown in **Figure 2**. The initial prepatterning of the Silicon wafer was achieved by depositing a monolayer of silica beads of radius 250 nm with standard lift off method. A subsequent electron beam evaporation of silver at an extreme angle to the wafer ensured the formation of metal islands at the top of the beads, which became spherical (of radius ≈ 70 nm) following a simple heating step. This resulted in the formation of a triangular array of metal nanoparticles of spacing 500 nm defined by the underlying array of silica beads, after which we used standard protocols to transfer a layer of chemical vapor deposition (CVD) grown graphene on the top of the array. This was followed by a similar procedure of depositing silver at an extreme angle and annealing it subsequently. The extreme angle of evaporation ensured the second layer of silver to be placed directly above the annealed silver nanosphere, separated by SLG. The substrate was cooled to liquid nitrogen temperatures during both the evaporation steps, such as to minimize the diffusion of the silver atoms. As seen from the scanning electron microscopy (SEM) images, i) the graphene layer remained well connected even after the entire fabrication process, implying its suitability for electrical transport measurements, although small amount of wear-and-tear in the SLG could also be seen and ii) the near spherical structure of the nanoparticle due to minimal wetting of graphene by silver during the deposition and/or annealing process. The imperfections were primarily caused by the defects in the arrangement of the underlying array of silica beads, although the quality of SLG grown by the CVD growth and structural damage during the transfer process was also important. It is important to note that the methods used in our fabrication were completely scalable, implying it will be possible to extend this process flow to wafer scale devices in future.

To make a quantitative estimate of the enhancement of the EM field, we measured the Raman scattering spectrum under normal incidence arising from the SLG sandwiched between the two arrays of silver nanoparticles. The strength of the Raman signals of the sandwiched SLG was much larger compared to bare SLG (without silver nanoparticles), as shown in the typical spectra shown in **Figure 3**a. The increase in width of the characteristic Raman bands for the sandwiched structure is related to the strains developed in graphene due to its (partially) suspended configuration, in agreement with studies reported[35] before. We took the ratio of the total area (A_G or A_{2D}) under each Raman band as an appropriate measure of the strength of the Raman signal. Accordingly, the ratio of the A_G (or A_{2D}) of the sandwiched structure to that of bare graphene provided an estimate of the plasmonic enhancement of the Raman

ADVANCED MATERIALS
www.advmat.de

www.MaterialsViews.com

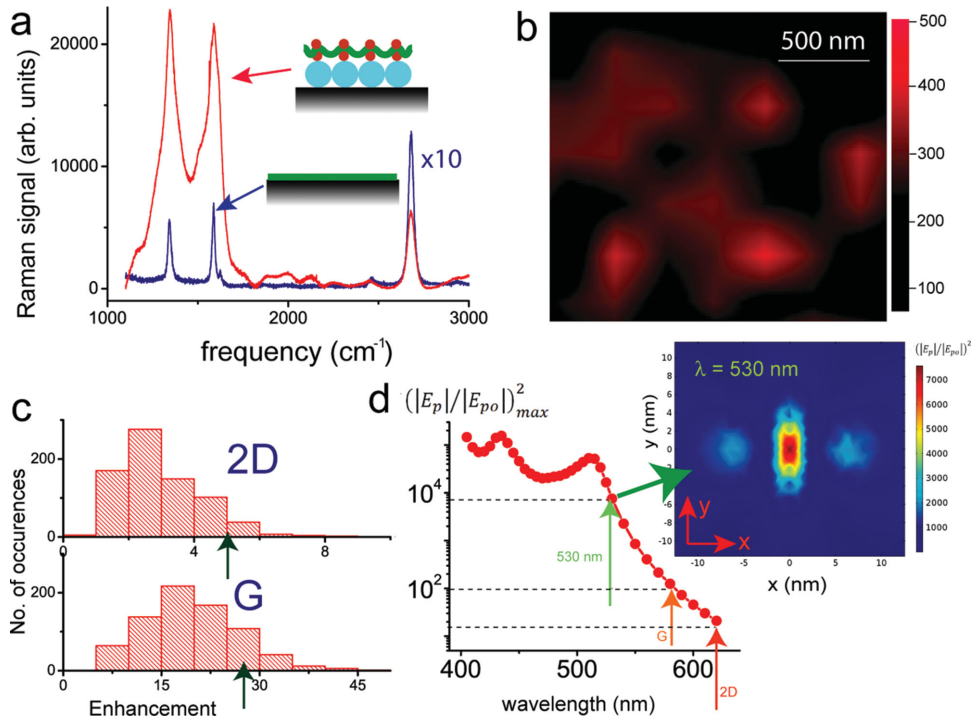

Figure 3. Raman measurements and EM field estimation. a) Typical Raman spectra of the SLG without (blue) and with the silver dimers (red). The spectra of the bare SLG sample (blue) have been multiplied by a factor of 10 for easier visual comparison. b) Map of the enhancement of the Raman signals for a particular Raman band (G). Although the contrast of the image was limited by the ratio of the size of the laser focus to the lattice spacing (500 nm) of the hot spots, a periodicity of ≈500 nm could be detected, implying the maximum Raman signal was probably arising at the nanoparticle junctions as per design. c) Histogram of the Raman enhancement for 2D (top) and G (bottom) bands, where we consider the area, arrows indicate the positions of the numerical estimate. d) Variation of $(|E_p|/|E_{po}|)^2_{max}$ with wavelength (λ). The wavelengths corresponding to the excitation laser (532 nm) and the emission (G – 580 nm and 2D – 621 nm) have been marked with arrows. (Inset) Showing the square of the parallel components of the enhanced EM fields, given by $(|E_p|/|E_{po}|^2)$, for illumination wavelength 530 nm, showing the strong confinement of the EM fields within a small region of area, $\sigma_p \approx 12$ nm^2. See the Supporting Information for details of estimation of σ_p. All dimensions are in nm.

signal, which was expected to be highest at the junction of the silver colloids, positioned directly above individual silica beads arranged in a hexagonal geometry. As shown in Figure 3c, a pattern[36] with approximate periodicity 500 nm of the Raman signal enhancement could be detected in the Raman map (G-band), implying the regions of maximum Raman enhancement indeed were formed at the top of the beads, as per the fabrication design. The contrast of the pattern was limited by the ratio of the diameter of the focal spot (≈720 nm) of the excitation laser to the periodicity of the pattern (500 nm), implying around 1.4 hot spots per measurement.

To verify that the observed increase in the Raman signal was indeed due to plasmonic enhancement, we estimate the strength of the EM field localized in each hot spot. We consider the distribution of the Raman signal enhancements for two Raman bands (2D and G), shown in Figure 3c. The enhancement was larger in the G band (20 ± 7.6) compared to 2D (3 ± 1.36), which could be understood by considering the mechanisms[21,35] leading to the enhancement of the Raman signal. The primary source of the enhancement was due to the component of the strongly enhanced near field parallel (E_p) to the SLG, amounting to $(|E_p|/|E_{po}|)^2_{abs} = 7543$ at the wavelength of the excitation laser (532 nm), as can be seen from the numerical simulations shown in Figure 3d. Note the largely enhanced EM fields were concentrated in a very small region of area $\sigma_p \approx 12$ nm^2 at the junction of the particles, as shown in Figure 3d. The secondary source of enhancement was due to the local electric enhancement at the Stokes-shifted emission wavelengths, which corresponded to $(|E_p|/|E_{po}|)^2_{emi} = 125$ (at 580 nm) and 21 (at 620 nm) for the G and the 2D bands, respectively. The net enhancement of the Raman signal for the laser focal spot of area $A = 0.4$ μm^2 was therefore given by $(|E_p|/|E_{po}|)^2_{abs}(|E_p|/|E_{po}|)^2_{emi}(\sigma_p/A)$, which amounted to be around 28 and 5 for the G and 2D bands, respectively. These values were reasonably close with the experimentally measured enhancements (20 ± 7.6 and 3 ± 1.36, respectively). Although the agreement was well, the large variability in the Raman signal (see the wide histograms shown in Figure 3c) merits some discussion. We believe this was due to the nonexact placement of the particles along the z-direction, something that was related to the spot to spot variability of the wafer scale fabrication scheme. This formed a source of experimental variability but could not be incorporated in the numerical model in any simple manner. The numerical model also neglected the nonlocal effects,[23–25] which could change the results to some extent. Accordingly the quantitative agreement between the numerical and experimental Raman signals should be considered as approximate.

While the Raman enhancement can be exploited in molecular sensing (using SERS) by functionalizing the sandwiched

DOI: 10.1002/adma.201404312

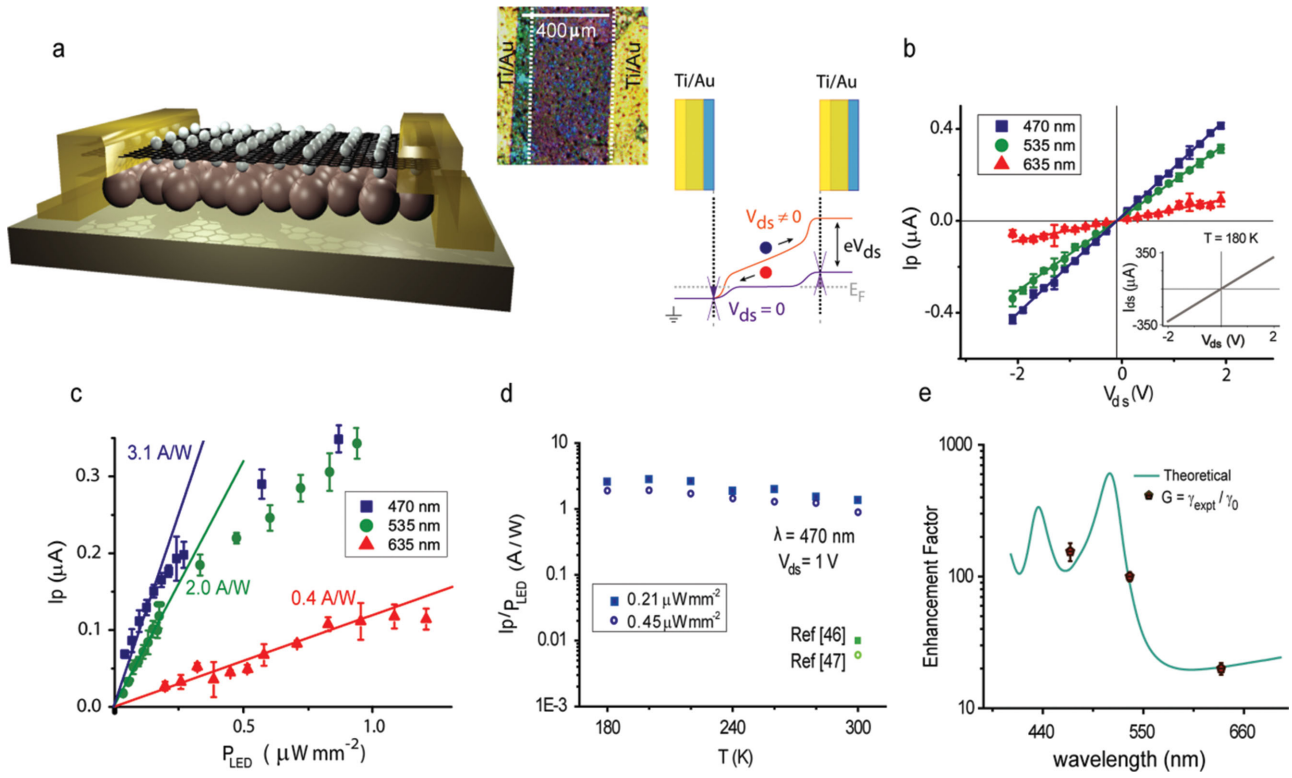

Figure 4. Photoresponse of graphene–nanoparticle dimer hybrid device. a) Left panel shows a device schematic, where graphene is sandwiched between dimers on silica beads on SiO_2 substrate. An optical image of the device is shown in the inset. The right panel illustrates bending of bands in our device by contacts and the source-drain bias (V_{ds}). b) The measured photocurrent for red (635 nm), green (535 nm), and blue (470 nm) photoillumination as a function of V_{ds} at 180 K. The error bars for each points are calculated from three similar measurement sequences. The solid lines are guide to the eye. Inset show the linear I_{ds}–V_{ds} characteristics in dark at T = 180 K. c) Symbols of different colors indicate measured photocurrent at V_{ds} = 1 V for different LED power of respective wavelengths. Solid lines indicate the regime where the photocurrent increases linearly with the power of illumination. d) Temperature dependent response (λ = 470 nm) for two values of illumination power is shown. The green solid square and the circle indicate previously reported responses obtained using plasmonic structures with graphene in refs. [46,47] respectively. e) Comparison of the computed and experimental photoresponse enhancement factor for different wavelengths. Error bars are obtained from three similar measurement schemes.

graphene, the double-layer structure also allows, as we demonstrate below, a new class of graphene–plasmonic photodetector with unprecedented sensitivity. Although several protocols ranging from nanostructuring[37] to hybridizing graphene with other semiconductors[38–41] are now available to overcome the intrinsically weak light response of the bare graphene photodetectors,[42,43] sensitizing graphene by coupling to plasmonic[44,45] structures offer the unique advantage of enhanced photoresponse without sacrificing the detection bandwidth. Recent experiments with lithographically[46] and thermally treated[47] metallic nanostructures imprinted onto exfoliated or CVD-grown graphene revealed over ten times increase in photoresponsivity in comparison to that of bare graphene at the resonant wavelengths. However the graphene channels in such devices were supported by insulating substrates and plasmonic enhancement was restricted only to the exposed side of graphene unlike the double-layer plasmonic focusing in the present case of graphene sandwiched between the nanoparticle dimers.

In order to evaluate the photoresponse of the graphene–silver dimer assembly titanium (Ti)–gold (Au) source and drain electrical contacts were shadow evaporated onto the assembly placed on insulting SiO_2 substrate (schematic in **Figure 4**a). As the micrograph in the inset of Figure 4a shows, our devices were macroscopically large (typical length ≈ 0.4 mm and width ≈ 0.8 mm), where the entire device area was illuminated (global illumination) with light emitting diodes (LEDs) of three different wavelengths centered around 470 nm (blue), 535 nm (green), and 635 nm (red). The source–drain current (I_{ds})–voltage (V_{ds}) characteristics of the device under both dark and illuminated conditions were both found to be linear with a nominal two-probe resistance of ≈5.7 kΩ (inset of Figure 4b). Figure 4b shows the photoresponse of the graphene–silver dimer hybrid for all three wavelengths recorded at 180 K at the same LED power level P_{LED} ≈ 0.51 μW mm^{-2} (see the Supporting Information for experimental details). Within the experimental range of $|V_{ds}| \leq 2$ V, the photocurrent $I_p = I_{light} - I_{dark}$, where I_{light} and I_{dark} are the measured source–drain currents in illuminated and dark conditions, respectively, varies linearly with V_{ds} irrespective of illumination wavelength. Maximum photocurrent as large as 400 nA was obtained for the blue illumination, which is about a factor of ten greater than that for red light emphasizing a strong wavelength selectivity. Our measurements with control devices of identical geometry where bare CVD graphene was laid directly onto the SiO_2 substrate yielded much weaker (≪10 nA) photocurrent when subjected to similar

excitations, implying that the large photoresponse to be directly associated with the presence of nanoparticle dimers.

While strong color-selectivity readily suggests the enhancement in the photoresponse to be due to plasmonic coupling of the EM radiation to graphene via the nanoparticle dimers, we discuss the possible mechanism of photosensitivity in our devices, which commonly arises from photovoltaic, photothermoelectric or bolometric processes.[48] A significant electron–hole asymmetry is unexpected in our simplistic two-probe device structure, where the entire layer of graphene is suspended on the array of metallic nanoparticles. This eliminates a significant contribution from the photothermoelectric effect.[49] Second, a photovoltaic effect due to the band bending (over a length scale of ≈200 nm) at the contacts,[42] as illustrated in the schematic of Figure 4a, arising from the work function difference at the contacts can lead to separation of the photogenerated electron–hole pairs.[42,50] In our devices, the contact-induced doping can be marginally asymmetric (Fermi energy shift ≈ 0.1 eV) due to slight shift of the Ti (mild electron doping) deposition with respect to Au (hole doping) during the shadow evaporation process (micrograph in Figure 4a). However, we found I_p to be zero at $V_{ds} = 0$ within experimental accuracy in all measurements (Figure 4b), confirming that the photogenerated carriers are generated and separated in the bulk of the graphene rather than at the contacts. This is indeed expected for nanoparticle dimer-mediated photoresponse, because the large inter-dimer separation (≈500 nm) in comparison to the spatial scale of band bending at the contacts makes EM field enhancement in contact region far less likely.

In electrically biased graphene photodetectors, both photovoltaic and bolometric processes can lead to photocurrent generation in the bulk. Since the graphene in our device is ungated and naturally suspended, it is exists close to the Dirac point where the photovoltaic effect via generation of nonequilibrium carriers is expected to dominate. This leads to photocurrent generation in the direction of the biasing current (positive photoresponse), as indeed observed in our experiment (Figure 4b). Assuming the photocurrent depends on the density n_e^* of the nonequilibrium carriers as $I_p = (W/L)eV_{ds}\,\mu n_e^*$,[48] the experimentally observed $I_p \approx 0.2$ μA at $V_{ds} = 1$ V and illumination power $P_{LED} = 0.25$ μW mm^{-2}, can be obtained with net external quantum efficiency of ≈1%, which is reasonable considering the highly disordered nature of the CVD graphene used in our experiments (carrier mobility $\mu \approx 100$ cm^2 V^{-1} s^{-1}). In fact, the temperature coefficient of conductivity in our devices is positive even at room temperature (see the Supporting Information), which indicates weak localization effects similar to that observed earlier in disordered CVD graphene,[51] and implies that the bolometric mechanism would also lead to a positive photoresponse in our devices. Note that this scenario is opposite to that observed for high mobility exfoliated graphene,[48] where the bolometric coefficient is negative due to the negative temperature coefficient of conductivity. However, since the bolometric effect dominates at higher (uniform) doping regime, it is expected to be weaker in our case, although cannot be ruled out entirely.

For further quantitative analysis of the photoresponse in our devices, we have measured I_p for all three colors as a function of the excitation power P_{LED} and temperature, keeping V_{ds} constant at 1 V. As shown in Figure 4c, I_p varies linearly with P_{LED} at small values of P_{LED} but becomes sub linear at larger P_{LED}. The deviation is maximum for blue illumination and minimum for red, suggesting that it is most likely a combined influence of screening[42] as well as local heating close to resonances frequencies. From the linearly varying regime, we find the photoresponsivity, $\gamma = I_p/P_{LED}$, can be as large as 3.1 A W^{-1} for blue illumination, but decreases by nearly a decade to 0.4 A W^{-1} for red light. Strikingly, this magnitude of γ is over 150–200 times larger than the previously constructed graphene–metal nanostructure assemblies,[46,47] making our devices most sensitive graphene plasmonic photodetectors. Moreover, the photoresponsivity is essentially temperature-independent well up to the room temperature (<60% variation) irrespective of excitation power (Figure 4d), which is in contrast to earlier graphene-based high-sensitivity photodetectors, where responsivity depends on temperature dependent physical properties of graphene such as the mobility.

Aside from high sensitivity, we also note several key distinctions between our graphene–nanoparticle dimer photodetectors and earlier plasmonic photodetctors based on graphene.[46,52] The fabrication of our devices is not only simple but naturally conducive to large-area scaling, involves only a single lithography-free metallization step and operates over a wide range of temperature (including room temperature) without a significant deterioration in performance. However, the CVD graphene channel is prone to damage (particularly while transferring on to the nanoparticle array) that may cause tears and ruptures giving rise to a large number potentials traps, particularly dangling bonds at the torn edges, voids etc. As a result, the response time (≈1 s) of our devices is significantly longer than common plasmonic devices based on high mobility graphene (see the Supporting Information), which can be attributed to charging of the traps by photogenerated carriers which degrades photoresponsivity dynamically. The charged traps increase the resistivity of the graphene channel thereby *reducing* the source drain current and hence act oppositely to the overall positive photoresponse due to plasmonic focusing. We emphasize this limiting influence of the charge traps in our case irrespective of the wavelength of photoexcitation, which is in contrast to the graphene–semiconductor nanoparticle hybrids where the nanoparticles assist in enhancing the photoconductivity by separating the photoexcited electrons and holes.[38] Nonetheless, it is remarkable that in spite of the deteriorating impact of the traps we could obtain such high photoresponsivities, suggesting a great scope of improvement in the performance of these graphene/dimer assemblies by carefully optimizing the growth and transfer process.

To investigate whether the strong EM field focusing by the metal dimer array is ultimately responsible for the enhanced photoresponse in our devices we numerically estimate the expected enhancement factor of the effective responsivity. Considering that experimentally observed γ depends on two factors: first, band bending caused by V_{ds}, and second, spatially averaged enhancement of the effective EM intensity, we can write,

$$\gamma(\lambda, V_{ds}) = \gamma_0(V_{ds}) \times \frac{1}{A_{cell}} \int\int_{cell} dx\,dy \left(\frac{E_\lambda}{E_{o\lambda}}\right)^2$$

Adv. Mater. 2015,
DOI: 10.1002/adma.201404312

where γ_0 (V_{ds}) is the responsivity of a bare graphene photodetector at the same level of band bending. The second factor on the right hand side of the above equation can be computed from the near field EM intensity enhancement (Figure 1c) and shown as the solid line in Figure 4e for a triangular lattice of dimers with mean distance of ≈500 nm (A_{cell} represents the area of a unit cell). We find a satisfactory agreement between the computed enhancement factor when the observed γ for each color shown in Figure 4c is scaled by $\gamma_0 \approx 20$ mA W^{-1}, which is typical for electrically biased graphene photodetectors and also close to the photoresponsivity estimated for our control devices of similar geometry. While the agreement should be considered qualitative, it indeed provides a strong support to the nanoparticle dimer-mediated plasmonic enhancement of photoresponse in graphene.

In conclusion, we have demonstrated a conceptually novel method to integrate plasmonic[53] nanoparticles with graphene, such as to achieve unprecedented EM field enhancement and photodetection sensitivity. The scalability of the entire process flow allow the development of large area devices, while the fabrication technique is general enough to be easily applicable to plasmonic nanoparticles of other sizes and materials (e.g., Gold, Aluminium, etc.), arrays of other 2D geometries, as well as other atomically thin spacers (e.g., MoS_2). This in turn may allow spectral tunability, necessary for both SERS and optoelectronic device applications, while engineering the coupling of plasmonic arrays at precise nm level separations could lead to photonic metamaterials with novel functionalities.

Experimental Section

Numerical Simulations: We used a commercial finite element based tool (COMSOL Inc.) for our numerical simulations. The 3D model geometry contained two silver nanoparticles (radius 70 nm) separated by 0.34 nm, surrounded by perfectly matched layer (PML) of thickness $\lambda/2$, was placed 2.5λ distance away the dimer. A dynamic tetrahedral meshing of ≈900 K mesh elements of maximum mesh element size of 4.5 nm and $\lambda/6$, and minimum mesh element sizes of 0.12 nm were chosen. The convergence of the code was checked by varying the fault tolerances. We also validated the numerical results against similar calculations reported[54] in the literature.

Fabrication Details: We cleaned a Si wafer (with top SiO_2 thickness of 285 nm) with acetone and isopropyl alcohol (IPA) and formed a mono layer of silica beads by the standard lift off method. The technique is based on our previous report[32] on the assembly of metallic islands on dielectric structures using OAD (oblique island deposition) in a commercial electron beam evaporator, where the normal to the substrate was at angle of 84° to the direction of incoming vapor. We have cooled[34] the substrate to liquid nitrogen temperatures for minimizing the diffusion of the metal atoms, and subsequently annealed[55,56] the substrate at 350 °C for about 25 min in Argon atmosphere, such as to obtain nearly uniform spheres. A single layer of CVD graphene was transferred on the substrate, following which a second layer of Ag was deposited by the same method (cooled OAD). The substrate is subsequently annealed at 200 °C for about 10 min to make the top layer of Ag particles spherical, thereby forming a dimer structure separated by SLG. SEM images taken in a time gap of few months were very similar, implying the device to be completely stable over time.

Raman Measurements: The Raman measurement was done using a "Horiba Jobin Yvon LabRAM HR Raman" instrument with the excitation wavelength at 532 nm using a 100X objective of numerical aperture (NA) = 0.9. The Raman map was done at a scan step increment of 300 nm with a laser power of approximately about 1.45 mW and an integration time of 3 s.

Supporting Information

Supporting Information is available from the Wiley Online Library or from the author.

Acknowledgements

The authors would like to acknowledge the National Nanofabrication Center (NNFC) and the Micro/Nano characterization Facility (MNCF) for the fabrication and characterization work done. The authors would also like to acknowledge the Department of Science and Technology, Government of India for the financial support under the Grant No. SR/S2/CMP-02/2007 and the TUE (Thermatic Unit of Excellence) project for development of nanoscience and technology, Space Technology Cell and Department of Biotechnology. This work is partially supported by the Ministry of Communication and Information Technology under a grant for the Centre of Excellence in Nanoelectronics, Phase II.

Received: September 17, 2014
Revised: December 19, 2014
Published online:

[1] S. A. Maier, *Plasmonics: Fundamentals and Applications: Fundamentals and Applications*, Springer, USA **2007**.
[2] L. Novotny, B. Hecht, *Principles of Nano-Optics*, Cambridge University Press, New York **2012**.
[3] K. Kneipp, Y. Wang, H. Kneipp, L. T. Perelman, I. Itzkan, R. R. Dasari, M. S. Feld, *Phys. Rev. Lett.* **1997**, *78*, 1667.
[4] S. Nie, S. R. Emory, *Science* **1997**, *275*, 1102.
[5] A. N. Grigorenko, M. Polini, K. S. Novoselov, *Nat. Photonics* **2012**, *6*, 749.
[6] M. P. Fleischmann, J. Hendra, A. J. McQuillan, *Chem. Phys. Lett.* **1974**, *26*, 163.
[7] H. J. Xu, M. Aizpurua, Käll, P. Apell, *Phys. Rev. E* **2000**, *62*, 4318.
[8] H. Xu, E. J. Bjerneld, M. Käll, L. Börjesson, *Phys. Rev. Lett.* **1999**, *83*, 4357.
[9] F. Liu, S. Kar, *ACS Nano* **2014**, *8*, 10270.
[10] E. Hao, G. C. Schatz, *J. Chem. Phys.* **2003**, *120*, 357.
[11] C. Vieu, F. Carcenac, A. Pépin, Y. Chen, M. Mejias, A. Lebib, L. Manin-Ferlazzo, L. Couraud, H. Launois, *Appl. Surf. Sci.* **2000**, *164*, 111.
[12] C. L. Haynes, R. P. Van Duyne, *J. Phys. Chem. B* **2001**, *105*, 5599.
[13] J. Kern, S. Großmann, N. V. Tarakina, T. Hackel, M. Emmerling, M. Kamp, J.-S. Huang, P. Biagioni, J. C. Prangsma, B. Hecht, *Nano Lett.* **2012**, *12*, 5504.
[14] J. J. Mock, R. T. Hill, A. Degiron, S. Zauscher, A. Chilkoti, D. R. Smith, *Nano Lett.* **2008**, *8*, 2245.
[15] J. Mertens, A. L. Eiden, D. O. Sigle, F. Huang, A. Lombardo, Z. Sun, R. S. Sundaram, A. Colli, C. Tserkezis, J. Aizpurua, S. Milana, A. C. Ferrari, J. J. Baumberg, *Nano Lett.* **2013**, *13*, 5033.
[16] D. M. O'Carroll, J. S. Fakonas, D. M. Callahan, M. Schierhorn, H. A. Atwater, *Adv. Mater.* **2012**, *24*, OP136.
[17] D. M. O'Carroll, C. E. Hofmann, H. A. Atwater, *Adv. Mater.* **2010**, *22*, 1223.
[18] C. Ciracì, R. T. Hill, J. J. Mock, Y. Urzhumov, A. I. Fernández-Domínguez, S. A. Maier, J. B. Pendry, A. Chilkoti, D. R. Smith, *Science* **2012**, *337*, 1072.

[19] A. C. Ferrari, *Solid State Commun.* **2007**, *143*, 47.
[20] A. C. Ferrari, J. C. Meyer, V. Scardaci, C. Casiraghi, M. Lazzeri, F. Mauri, S. Piscanec, D. Jiang, K. S. Novoselov, S. Roth, A. K. Geim, *Phys. Rev. Lett.* **2006**, *97*, 187401.
[21] F. Schedin, E. Lidorikis, A. Lombardo, V. G. Kravets, A. K. Geim, A. N. Grigorenko, K. S. Novoselov, A. C. Ferrari, *ACS Nano* **2010**, *4*, 5617.
[22] W. Xu, X. Ling, J. Xiao, M. S. Dresselhaus, J. Kong, H. Xu, Z. Liu, J. Zhang, *Proc. Natl. Acad. Sci. USA* **2012**, *109*, 9281.
[23] G. Toscano, S. Raza, A.-P. Jauho, N. A. Mortensen, M. Wubs, *Opt. Express* **2012**, *20*, 4176.
[24] T. Teperik, P. Nordlander, J. Aizpurua, A. Borisov, *Phys. Rev. Lett.* **2013**, *110*, 263901.
[25] G. Toscano, S. Raza, S. Xiao, M. Wubs, A.-P. Jauho, S. I. Bozhevolnyi, N. A. Mortensen, *Opt. Lett.* **2012**, *37*, 2538.
[26] B. B. Dasgupta, R. Fuchs, *Phys. Rev. B* **1981**, *24*, 554.
[27] F. J. García de Abajo, *J. Phys. Chem. C* **2008**, *112*, 17983.
[28] R. Esteban, A. G. Borisov, P. Nordlander, J. Aizpurua, *Nat. Commun.* **2012**, *3*, 825.
[29] D. C. Marinica, A. K. Kazansky, P. Nordlander, J. Aizpurua, A. G. Borisov, *Nano Lett.* **2012**, *12*, 1333.
[30] K. J. Savage, M. M. Hawkeye, R. Esteban, A. G. Borisov, J. Aizpurua, J. J. Baumberg, *Nature (London)* **2012**, *491*, 574.
[31] N. A. Mortensen, S. Raza, M. Wubs, T. Søndergaard, S. Bozhevolnyi, *Nat. Commun.* **2014**, *5*, 3809.
[32] H. Johnson Singh, A. Ghosh, *J. Phys. Chem. C* **2012**, *116*, 19467.
[33] M. M. Hawkeye, M. J. Brett, *J. Vac. Sci. Technol. A* **2007**, *25*, 1317.
[34] A. G. Mark, J. G. Gibbs, T.-C. Lee, P. Fischer, *Nat. Mater.* **2013**, *12*, 802.
[35] S. Heeg, R. Fernandez-Garcia, A. Oikonomou, F. Schedin, R. Narula, S. A. Maier, A. Vijayaraghavan, S. Reich, *Nano Lett.* **2013**, *13*, 301.
[36] Z. Fang, Z. Liu, Y. Wang, P. M. Ajayan, P. Nordlander, N. J. Halas, *Nano Lett.* **2012**, *12*, 3808.
[37] Y. Zhang, T. Liu, B. Meng, X. Li, G. Liang, X. Hu, Q. J. Wang, *Nat. Commun.* **2013**, *4*, 1811.
[38] G. Konstantatos, M. Badioli, L. Gaudreau, J. Osmond, M. Bernechea, F. P. G. de Arquer, F. Gatti, F. H. L. Koppens, *Nat. Nanotechnol.* **2012**, *7*, 363.
[39] C.-H. Liu, Y.-C. Chang, T. B. Norris, Z. Zhong, *Nat. Nanotechnol.* **2014**, *9*, 273.
[40] K. Roy, M. Padmanabhan, S. Goswami, T. P. Sai, G. Ramalingam, S. Raghavan, A. Ghosh, *Nat. Nanotechnol.* **2013**, *8*, 826.
[41] D. Zhang, L. Gan, Y. Cao, Q. Wang, L. Qi, X. Guo, *Adv. Mater.* **2012**, *24*, 2715.
[42] T. Mueller, F. Xia, P. Avouris, *Nat. Photonics* **2010**, *4*, 297.
[43] F. Xia, T. Mueller, Y. Lin, A. Valdes-Garcia, P. Avouris, *Nat. Nanotechnol.* **2009**, *4*, 839.
[44] X. Yu, J. Tao, Y. Shen, G. Liang, T. Liu, Y. Zhang, Q. J. Wang, *Nanoscale* **2014**, *6*, 9925.
[45] X. Zhu, L. Shi, M. S. Schmidt, A. Boisen, O. Hansen, J. Zi, S. Xiao, N. A. Mortensen, *Nano Lett.* **2013**, *13*, 4690.
[46] T. J. Echtermeyer, L. Britnell, P. K. Jasnos, A. Lombardo, R. V. Gorbachev, A. N. Grigorenko, A. K. Geim, A. C. Ferrari, K. S. Novoselov, *Nat. Commun.* **2011**, *2*, 458.
[47] Y. Liu, R. Cheng, L. Liao, H. Zhou, J. Bai, G. Liu, L. Liu, Y. Huang, X. Duan, *Nat. Commun.* **2011**, *2*, 579.
[48] M. Freitag, T. Low, F. Xia, P. Avouris, *Nat. Photonics* **2013**, *7*, 53.
[49] X. Xu, N. M. Gabor, J. S. Alden, A. M. van der Zande, P. L. McEuen, *Nano Lett.* **2009**, *10*, 562.
[50] X. Wang, W. Xie, J. Du, C. Wang, N. Zhao, J. Xu, *Adv. Mater.* **2012**, *24*, 2614.
[51] A. N. Pal, A. A. Bol, A. Ghosh, *Appl. Phys. Lett.* **2010**, *97*, 133504.
[52] M. Freitag, T. Low, W. Zhu, H. Yan, F. Xia, P. Avouris, *Nat. Commun.* **2013**, *4*, 1951.
[53] H. A. Atwater, A. Polman, *Nat. Mater.* **2012**, *9*, 205.
[54] I. Romero, J. Aizpurua, G. W. Bryant, F. J. García de Abajo, *Opt. Express* **2006**, *14*, 9988.
[55] G. Nair, H. J. Singh, D. Paria, M. Venkatapathi, A. Ghosh, *J. Phys. Chem. C* **2014**, *118*, 4991.
[56] J. H. Singh, G. Nair, A. Ghosh, A. Ghosh, *Nanoscale* **2013**, *5*, 7224.

Adv. Mater. **2015**,
DOI: 10.1002/adma.201404312